Interior Noise Reduction Method of Pantograph Areas for High-speed Trains Based on Active Jet Technology

D. Liu[1], X. Miao[1†], Z. Zhang[1], J. Yang[2], T. Yuan[2] and R. Song[2]

[1.] *School of Mechanical and Automotive Engineering, Shanghai University of Engineering Science, 201620, China*
[2.] *School of Urban Railway Transportation, Shanghai University of Engineering Science, 201620, China*

†Corresponding Author Email: 01120003@sues.edu.cn

ABSTRACT

The interior noise caused by the pantograph area is greater than that caused by other areas, and the impact of this pantograph area becomes more significant as the speed of high-speed trains increases, especially above 350 km/h. This study proposes an active jet method for pantograph cavities to control noise at the source. First, a predictive model for the interior noise of pantograph carriages was established by jointly adopting large eddy simulation–statistical energy analysis methods. Then, numerical simulations were conducted to determine the external noise sources and interior sound pressure level at different speeds (300, 350, 400, and 450 km/h). Finally, active jets at different speeds (97.2, 111.1, 125, and 140 m/s) were used to analyze the reduction in interior noise. Results showed that the active jet method decreased the average overall sound pressure level of the acoustic cavity in the horizontal plane. When the train speed reached 450 km/h, the optimal reduction in interior noise was approximately 7.5 dB in the horizontal plane for both the standing and sitting postures. The proposed method can efficiently reduce interior noise in the pantograph area.

1. INTRODUCTION

The operating speed of high-speed trains has been increasing in recent years, leading to a growing issue of aerodynamic noise. Previous studies have shown that when train speeds exceed 350 km/h, the aerodynamic noise surpasses the wheel–rail noise, accounting for more than 50% of the total train noise (Schetz, 2001; Thompson et al., 2015; Zhu et al., 2021). As the speed of a high-speed train increases, the aerodynamic noise increases by six to eight times the vehicle speed, which exacerbates noise pollution in the external environment and affects the comfort of passengers inside the carriage (Lu, C. et al., 2023b). Therefore, the research and optimization of aerodynamic noise control technology is an important performance index for high-speed trains.

Among the various sources of aerodynamic noise, the pantograph area significantly affects the interior noise. Many scholars have studied the interior noise of pantograph areas. Guo et al. (2017) measured the interior noise in a pantograph area and determined the values to be significantly greater (approximately 1 kHz) than those in other areas. Zhang, et al. (2019) studied the interior noise

of high-speed trains under different driving conditions and found that the interior noise level at the end of the pantograph compartment is more easily affected by the pantograph area. Chen et al. (2012) measured noise and vibrations near and farther away from the pantograph and revealed this area to be the main aerodynamic sound source, with vibrations transmitting noise inside the train through the roof. Li et al. (2022) used the waveguide boundary element method and performed experiments and found that the sound pressure level (SPL) was greater at the roof under the pantograph. Lee et al. (2022) utilized large-eddy simulation (LES) and the wavenumber spectrum to calculate compressible and incompressible pulsating pressures as excitation sources via finite element analysis, followed by statistical energy analysis (SEA) modeling to predict interior noise levels in cars. Yang et al. (2013) combined LES and SEA to obtain the aerodynamic noise spectrum inside the head of a train and applied pulsating pressure on the head surface as the excitation source.

High-speed trains mainly transmit internal noise into the passenger compartment in two ways, namely, airborne and structural propagation, which can also be categorized as noise excitation and vibration excitation, respectively

Nomenclature			
t	time	$\bar{p}$	filtered pressure
ρ	density	u_i, u_j	filtered speed
v	kinematic coefficient of viscosity	f_c	critical frequency
ω	frequency	c	velocity of sound
P_I	input energy	D	thickness
η_{ij}	coupling loss factor	E	Young's modulus
η_i	internal loss factor	σ	Poisson's ratio
n_i	modal density	SPL	Sound Pressure Level
E_i	energy stored by the subsystem	OSPL	Overall Sound Pressure Level

([Kim & Kim 2011](#)). [Yao et al. (2022)](#) analyzed the complex structure of a pantograph by wrapping the insulators and base frame and determined that only the modified base frame could significantly reduce noise. [Cao et al. (2018)](#) performed a numerical simulation and reported that vortex shedding on rods, particularly on the pantograph bow head, was responsible for the aerodynamic noise; they also designed a bow head with a bionic feather structure and achieved a maximum noise reduction of 10 dB at each observation point. [Li et al. (2023)](#) investigated the application of porous sound-absorbing materials (e.g., high-speed train body structures) as double-panel structures to limit the internal vibration noise caused by flow; their acoustic optimization design reduced sound transmission in the body by approximately 5.2 dB. [Zhang et al. (2022)](#) designed a lightweight low-frequency acoustic material (e.g., bunching resonator) to effectively control the low-frequency noise and vibration of a compartment plate. [Wang et al. (2020)](#) proposed a signal reconstruction-based active noise control algorithm for train internal noise, which not only effectively suppressed the internal noise but also avoided pollution from secondary sound sources.

However, analyses of interior noise resulting from pantograph aerodynamic noise and from efficient interior noise reduction methods are still limited. Consequently, this study explored an active jet interior noise reduction method by focusing on the interior noise source from pantograph aerodynamic noise. The standard k–ε model and LES method were utilized. The pulsating pressure in the turbulent boundary layer (TBL) was calculated as the aerodynamic excitation source of the pantograph cavity, and the interior noise was calculated based on the SEA method.

2. NUMERICAL METHOD

2.1. Large-Eddy Simulation

The LES method states that turbulent motion consists of vortices of different scales in which the large-scale turbulent fluctuations contain the majority of the energy and momentum. These large-scale fluctuations dominate the transport of momentum and energy within the vortices, whereas small-scale fluctuations influence the dissipation of turbulent kinetic energy ([Kolmogorov, 1991](#)). The LES method utilizes a filtering function to decompose instantaneous turbulent motion into two components: large-scale vortices and small-scale vortices. The large-scale vortices are numerically solved using the N–S governing equation after filtering (Eq. [2]), whereas the small-scale vortices are simulated using subgrid-scale models. The function of the filter is to smooth the flow

field in space or time; it filters out small-scale details in the fluid, leaving only the large-scale turbulent vortex structure. Filters, which usually include a filtering function and a filtering operation, also decompose the flow field into scale-based components. Subsequently, each variable is divided into two parts. The filtered variables include the following:

$$\bar{\phi} = \int_D \phi G(x, x') d_x \tag{1}$$

Where $\bar{\phi}$ is the filtered variable and D is the flow region; $G(x, x')$ is a filter function from which the scale of the solved vortex is determined.

The filtered N-S governing equation is given by:

$$\frac{\partial}{\partial t}(\bar{u}_i) + \frac{\partial}{\partial x_j}(\bar{u}_i \bar{u}_j) = -\frac{1}{\rho}\frac{\partial \bar{p}}{\partial x_i} + v\frac{\partial^2 \bar{u}_i}{\partial x_j \partial x_j} - \frac{\partial \tau_{ij}}{\partial x_j} \tag{2}$$

$$\frac{\partial \bar{u}_i}{\partial x_i} = 0 \tag{3}$$

Where $\bar{u}_i$、 $\bar{u}_i$ denotes the filtered speed, m/s; $i \neq j = 0,1,2$; t denotes the time, s; ρ denotes the density, m/s; $\bar{p}$ denotes the filtered pressure, p_a; v denotes the kinematic viscosity coefficient, m^2/s; and τ_{ij} is the sublattice scale stress, which is given by $\rho\overline{u_i u_j} - \rho\bar{u}_i \bar{u}_j$. The effect of small-scale vortex motion on large-scale vortex motion is solved using a sublattice scale model, in which sublattice scale stress (τ_{ij}) is the key physical quantity of the model used to reflect the degree of influence of small-scale vortex on the above mentioned governing equation.

2.2. Statistical Energy Analysis

The SEA method for describing system vibration applies the concept of vibration energy. This approach enables the study of dynamic response and vibration acoustic radiation in complex systems from an energy perspective. The SEA model is particularly useful for calculating the dynamic response and vibration acoustic radiation of complex structures subjected to high wide-band random loads. The fundamental principle of SEA involves dividing a complex system into a series of interconnected subsystems. The energy flow relationships between different subsystems are established based on the system parameters from which the energy balance equation of the system is derived. Then, the energy, vibration response, and vibration acoustic radiation of each subsystem are calculated using the energy balance equation. A subsystem is defined as a finite region with similar resonance characteristics. The energy of a subsystem primarily depends on external input excitation, power loss, and power exchange. The core equation of
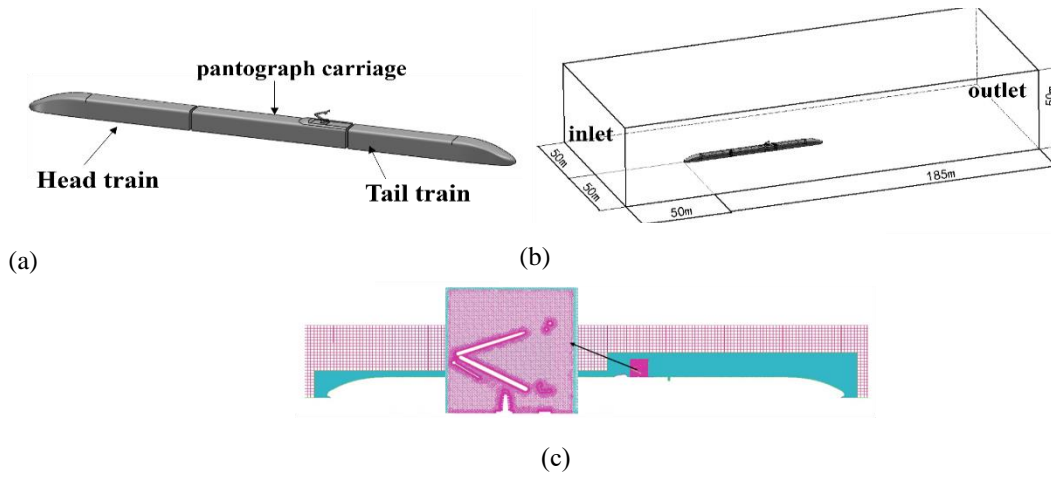
Fig. 1 CFD model (a) Three-carriages train model (b) computational domain of the external flow field (c) Schematic of the body mesh cross-section in the computational domain

SEA is the power flow balance equation, which states that the input power flow of a subsystem equals the sum of the power loss flow within the subsystem and the power transfer flow between the subsystem and other subsystems (Burroughs et al., 1997). For a system with m subsystems, the power flow balance equation is expressed as:

$$\omega \begin{pmatrix} \eta_{11}n_1 & -\eta_{12}n_1 & \cdots & -\eta_{1m}n_1 \\ -\eta_{21}n_2 & \eta_{22}n_2 & & -\eta_{2m}n_2 \\ \vdots & & \ddots & \vdots \\ -\eta_{m1}n_m & -\eta_{m2}n_m & \cdots & \eta_{mm}n_m \end{pmatrix}$$

$$\begin{pmatrix} E_1/n_1 \\ E_2/n_2 \\ \vdots \\ E_m/n_m \end{pmatrix} = \begin{pmatrix} p_1 \\ p_2 \\ \vdots \\ p_m \end{pmatrix} \quad (4)$$

$$\eta_{ii} = \eta_i + \sum_{j=1, \ j \neq 1}^{m} \eta_{ij} \quad (5)$$

Where ω represents the frequency, Hz; P_I indicates the input energy, N/m; η_{ij} represents the coupling loss factor of subsystem i to j; η_i represents the internal loss factor; n_i represents the modal density, s/rad; and E_i represents the energy stored by the subsystem, N/m.

3. PREDICTIVE MODEL OF AERODYNAMIC NOISE IN PANTOGRAPH CARRIAGE

3.1. Details of the CFD Model and Simulation

Figure 1(a) shows a 1:1 scale model with three carriages: head train, pantograph carriage, and tail train. This scale model was used to realistically simulate the external flow field of the train. The above 3D model was completed in SolidWorks software. The operating conditions of the single vehicles were set to bright lines, and the train height was set to a characteristic height of 3.74 m. According to the Train Aerodynamic Simulation Standard of China (TB/T 3503.4-2018), the height of the calculation domain should not be less than 8 times the characteristic height, the distance between the entrance border and the front should not be less than 8 times the characteristic height, and the distance between the rear and the exit border should not be less than 16 times the characteristic height. Figure 1(b) shows the computational

domain of high-speed train aerodynamics, with the left and right sides corresponding to the speed inlet boundary and pressure outlet boundary, respectively. The pressure was set to 0 Pa. The bottom and car body were set as fixed walls, and the two sides and the top were set as symmetric boundaries. The left and right sides of the train have similar aerodynamic and flow characteristics.

The structure of the pantograph area and the head and tail areas of high-speed trains are complicated in terms of the mode. In the meshing process in this study, unstructured and structured grids were combined to divide the grid by ICEM CFD. In the whole computing domain, the division scheme of the unstructured grid and the unstructured- and grid-structured grid was applied from inside to outside. An unstructured grid was used in the pantograph, another unstructured grid was used outside the train, and structural grids constituted the remaining parts of the final outflow field. Five groups of grids were prepared for the independence test (Table 1). When the total number of grids was 30,723,300, the number of grids continued to increase, but the maximum acoustic power on the train surface did not change significantly. In the fourth grid, the minimum grid size of the pantograph area was 17 mm, the minimum mesh size of the train surface was 40 mm, and the grid size of the flow field area was 50 mm. Thus, the fourth grid scheme was adopted for all the simulation calculations. The distribution of the spatial grid is shown in Fig. 1(c).

The current simulation was performed using the commercial software ANSYS Fluent 2020. The solver setup for CFD was divided into two steps. First, the standard k–ε model was used to calculate the steady-state flow field of the high-speed train. The calculation step size was set to 500 steps. Second, with the steady-state flow field taken as the initial value, the transient flow field of the high-speed train was simulated using the LES method. According to Nyquist's theorem, the highest frequency of noise analysis can be determined based on the time step. According to noise analysis, the highest frequency is $1/(2T)$ when the time step is T. Here, the maximum noise frequency of the high-speed train is 5000 Hz. The value was obtained based on the transient flow field calculation time step of 0.0001 s, with a total calculation time of 0.2 s. Table 2 shows the specific solution method. The aerodynamic simulation results were validated by

Table 1 Grid independence verification

Mesh	Mesh points (million)	First layer thickness (mm)	Number of prism layers	Minimum size (mm)	Stretching ratio	Maximum acoustic power level(dB)
1	18.8931	0.08	5	1	1.1	137.58
2	22.0468	0.08	5	0.9	1.1	136.35
3	25.0672	0.08	5	0.8	1.1	135.86
4	30.7233	0.08	5	0.8	1.1	135.77
5	32.6290	0.08	5	0.8	1.1	135.95

Table 1 Solution method

type	Steady calculation(k-ε model)	Transient calculation(LES)
solver	Pressure Based	Pressure Based
Pressure correction algorithm	SIMPLEC	SIMPLEC
Gradient dispersion	Least Squares Cell Based	Least Squares Cell Based
Pressure dispersion	Second Order Upwind	Second Order Upwind
Momentum discrete method	Second Order Upwind	Bounded Central Differencing

(a)   (b)
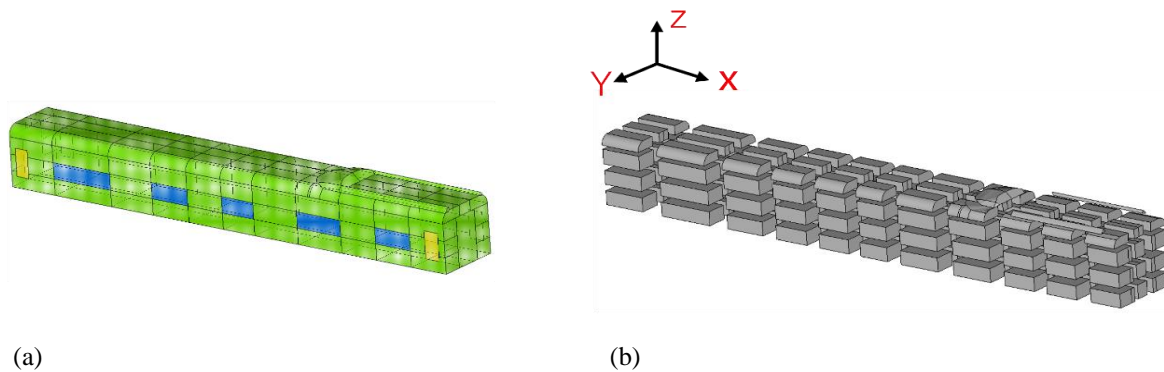
Fig. 2 SEA model: (a) Pantograph body structure subsystem (b) Interior acoustic cavity subsystem

previous aerodynamic simulation and wind tunnel experiment (Guo et al., 2023).

3.2. Details of the SEA Model and Simulation

Given the large size of the train model, the quadrilateral mesh on the train surface was divided into a minimum size of 50 mm by HyperMesh software. The whole pantograph carriage was also divided into SEA subsystems according to the mesh nodes on the carriages in VA One software. Following the principle of subsystem division, the surface of a compartment can be divided into different plate subsystems based on the regions with different material properties (i.e., body, doors, and windows). Figure 1(a) shows the surface of the pantograph compartment divided into three types: the green part for the frame of the aluminum body, the blue part for the tempered glass, and the yellow part for the door. The respective material and physical properties are also shown in the figure.
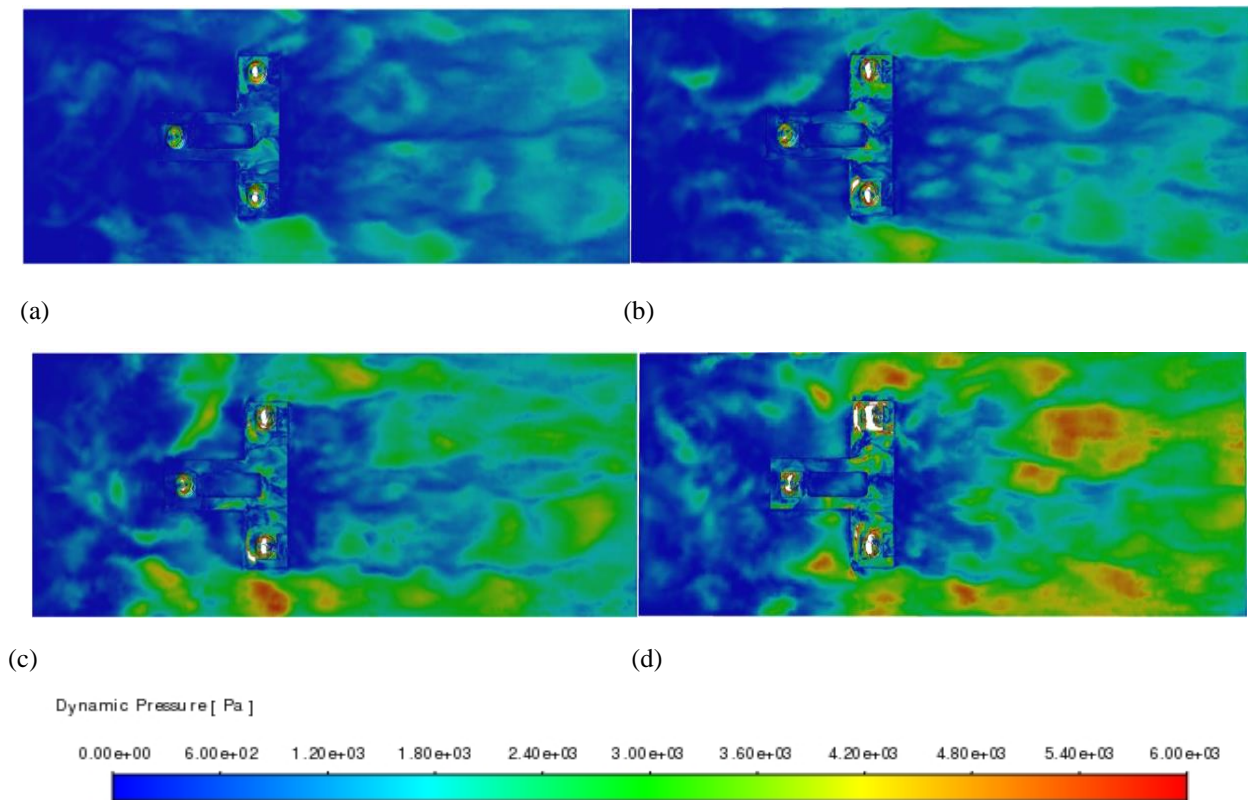
The acoustic cavity subsystem inside the carriage is a closed space composed of a body structure subsystem and an interior auxiliary flat panel. The sound intensity in all parts of the train is inconsistent because of the different postures of passengers. Here, in the X-direction, the bridge was divided into 12 sections based on the window and door configurations. In the Y-direction, the body was divided into three sections based on the seat and corridor

configurations. In the Z-direction, the body was divided into four sections based on the location of the luggage racks and the standing, sitting, and squatting postures with respect to the height of the human body. In addition, together with the three acoustic cavity subsystems of the pantograph deflector, 247 acoustic cavity subsystems were established inside the carriage (Fig. 2[a]).

The main parameters of the SEA method included the modal density, subsystem internal loss factor, and coupling loss factor in Eqs. (4) and (5). The theoretical formulas in the literature were used to obtain the modal density of each subsystem, the loss factor, and the coupling loss factor between different subsystems (Zhang et al., 2016; Henry & Thebaud 2016). Then, on the basis of the constructed SEA model, the pulsating pressure on the bottom of the cavity was applied to the "plate" of the constructive model in the form of a TBL.

4. ACQUISITION OF EXTERNAL EXCITATION SOURCE AND PREDICTION OF INTERIOR AERODYNAMIC NOISE

The standard k–ε model and LES were used to numerically calculate the external flow field of the train at

(a)   (b)

(c)   (d)

Dynamic Pressure [Pa]

0.00e+00   6.00e+02   1.20e+03   1.80e+03   2.40e+03   3.00e+03   3.60e+03   4.20e+03   4.80e+03   5.40e+03   6.00e+03

Fig. 3 Contours of pulsating pressure at the bottom of the cavity: (a) 300 km/h; (b) 350 km/h; (c) 400 km/h; (d) 450 km/h

different train speeds (300, 350, 400, and 450 km/h). The pulsating pressure spectra at the bottom of the cavity were calculated to analyze the change trend of the pulsating pressure at these different train speeds. The pulsating pressure was considered the interior noise excitation source. Then, the SEA method, whose apparatus was positioned directly under the pantograph, was utilized to predict the SPL inside the train. The change trends of the interior sound pressure at different train speeds were also analyzed.

### 4.1. Turbulent Pulsating Pressure on the Bottom of Pantograph Cavity

Figure 3 shows the pulsating pressure distribution range of the bottom wall of the pantograph cavity. This scheme allowed the simulation to be viewed more effectively from a qualitative perspective. The contours of the pulsating pressure on the bottom of the cavity at different train speeds (300, 350, 400, and 450 km/h) were also determined. Comparative analyses of Figs. 3(a) to (d) indicate that the pulsating pressure is the main contributor to the pressure around the insulators. With increasing speed, the distribution range and numerical scale also increased. The airflow directly affects the edges of the pantograph insulators and the bottom plate of the cavity, causing a greater pulsating pressure. The interaction between the airflow and air viscosity led to the formation of a TBL on the cavity bottom wall. The thickness of this boundary layer increased along the longitudinal direction of the train. Additionally, the vortices within the boundary layer continually affected the wall surface, leading to a greater distribution range and numerical scale of pulsating pressure behind the insulator than at the front.

The bottom wall was divided into nine uniform equal sections to ensure that the pulsating pressure at the bottom of the cavity would match the pressure at the bottom plate of the cavity on the SEA model (Fig. 4[a]). Given the low and uneven distribution of the pulsating pressure on the wall in front of the insulator in the cloud diagram, faces 1 to 3 were combined in the calculation. The findings are shown in Fig. 5. Within the analyzed frequency range of 16–5000 Hz, the pulsating pressure values for frequencies 1–3 and 5 exhibited a decreasing trend with increasing frequency.

A comparative analysis of Figs. 5(a) and (b) reveals that the pulsating pressure spectrum of the rear of the insulator is larger than that of the front of the insulator under the same train speed conditions at one-third octave. When high-speed air flows through the insulator and the bottom of the cavity, it is distributed into large and small vortices by the complex structure, and these vortices hit the wall at the back of the insulator. Along the longitudinal direction of the train, the thickness of the TBL on the wall of the cavity and the pressure increased. In summary, the pulsating pressure spectrum at the back of the insulator was greater than that at the front.

4.2. Interior Noise Underneath the Pantograph

As described in Section 3, the interior area underneath the pantograph within the carriage was divided into four blocks in the Z-direction, three blocks in the X-direction, and three blocks in the Y-direction, for a total of 36 acoustic cavities. These acoustic cavities are numbered 1 to 9 in the horizontal plane, as shown in Fig. 4(a). In the Z-direction, two horizontal planes in the middle of the

(a)   (b)
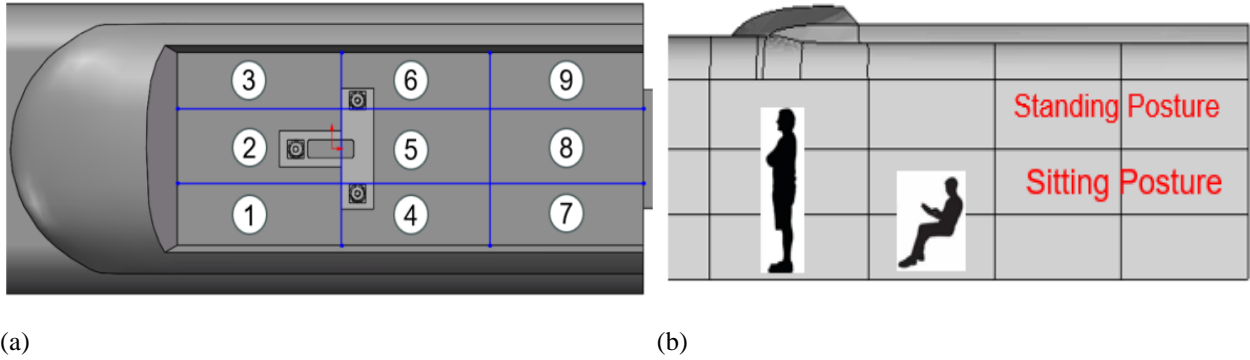
Fig. 4 Schematic segmentation: (a) Bottom (b) Split view of pantograph carriages

(a)   (b)
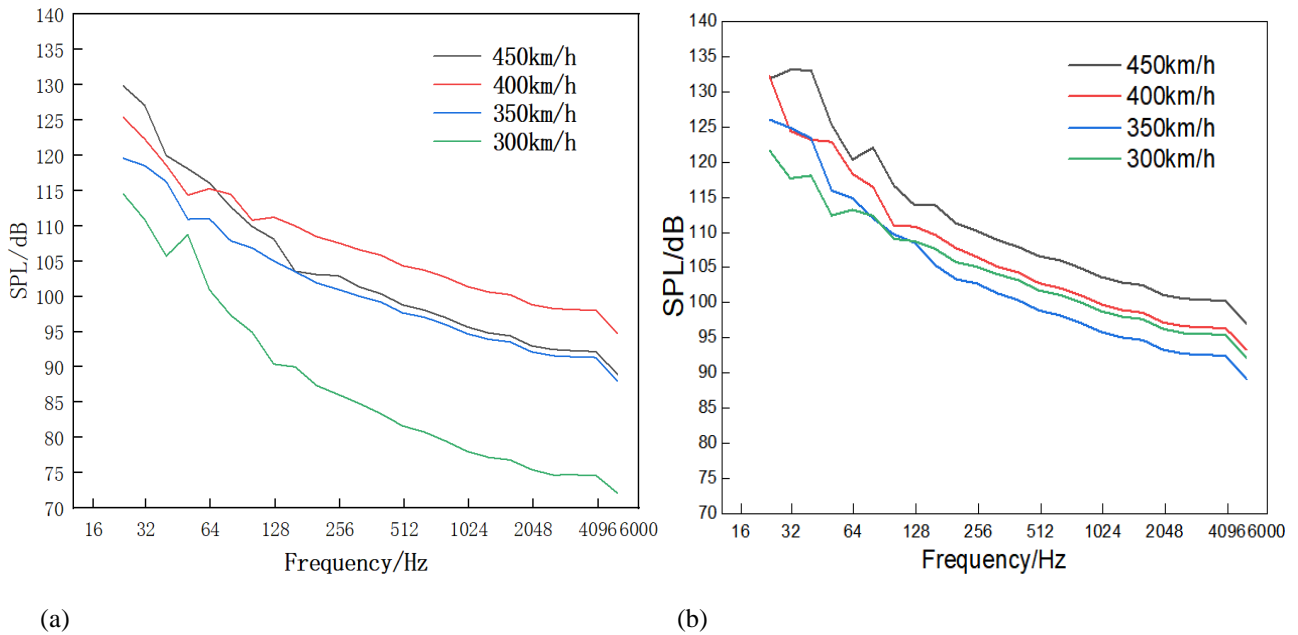
Fig. 5 Pulsating pressure spectrum at the bottom of the pantograph cavity: (a) Front of insulator: 1~3

(b) Back of the insulator: 5

train were considered, corresponding to the standing and sitting postures of the passenger (Fig. 4[b]). The standing posture on the left of the horizontal plane and the sitting posture on the right were taken as the research objects; they represent the second layer (sitting posture) and the third layer (standing posture) from the bottom to the top at 1 and 1.5 m, respectively.

As shown in Figs. 6(a) and (b), the SPLs of the acoustic cavities for standing posture no. 5 and sitting posture no. 5 increase with increasing train speed but decrease with increasing frequency in the ranges of 16–1000 and 1250–5000 Hz, respectively. The SPLs of both the cavities for standing posture no. 5 and sitting posture no. 5 increased abruptly at 1000–1250 Hz and decreased gradually. On the longitudinal coordinate, the spectral SPL in the sound cavity in the standing posture (Fig. 6[b])

was approximately 20 dB greater than that in the sitting posture (Fig. 6[a]) under the same vehicle speed conditions.

The structural model of the train body system consisted of aluminum plates with a thickness of 0.01 m. The critical fitting frequency of a veneer was 1243 Hz,

calculated from Eq. (6) for coincidence frequency; this value is within the range of sudden changes in the SPL spectrum. The wavelength of the bending wave of the plate was evaluated according to its elastic properties. In this manner, the conditions causing the coincidence effect could be determined on the basis of the frequency and angle of incidence of the sound wave. The critical frequency (fc) of the coincidence effect is defined as：

$$f_c = \frac{c^2}{2\pi \sin^2\theta} \sqrt{\frac{12\rho(1-\sigma^2)}{ED^2}} \qquad (6)$$

where c denotes the velocity of sound, m/s; D denotes the thickness, m; ρ denotes the density, which refers to the density of the aluminum veneer, kg/m^3; E denotes the Young's modulus, N/m^2; and σ denotes the Poisson's ratio. According to the literature (Chen et al., 2016), when the frequency reaches the anastomosing effect zone of the structure, the sound insulation of the panels decreases with increasing frequency.

Figures 7(a) and (b) show the overall SPL (OSPL). The OSPL of the acoustic cavities inside the carriage increased with increasing speed on the horizontal plane
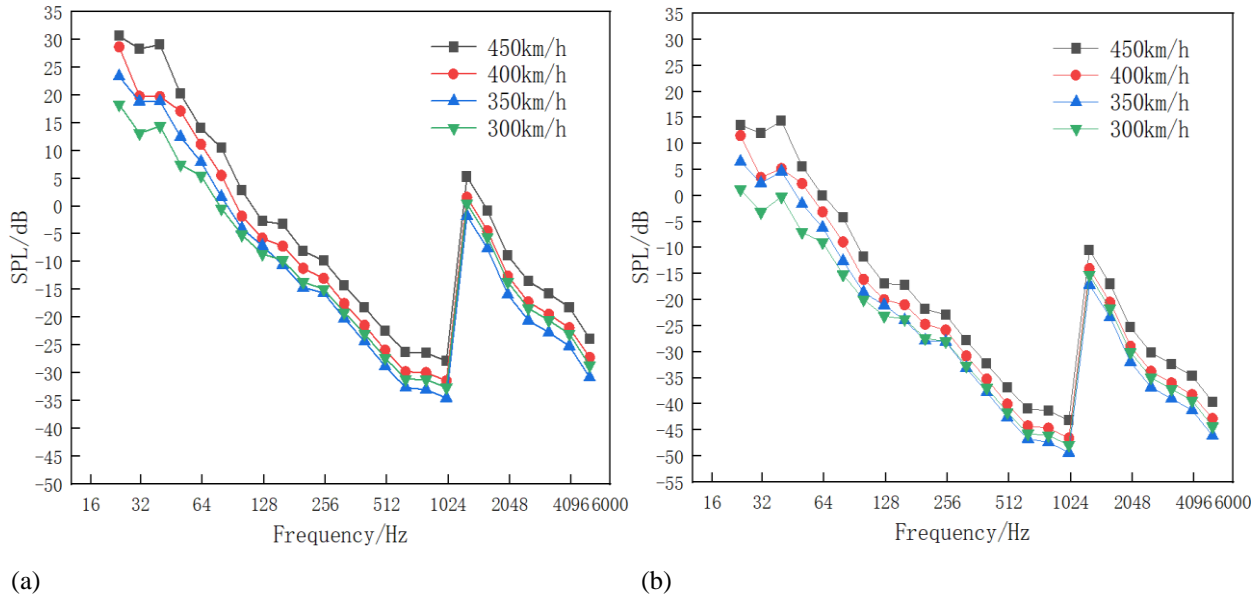
Fig. 6 Spectrum of sound pressure level: (a) Standing posture, acoustic Cavity 5 (b) Sitting posture, acoustic Cavity 5
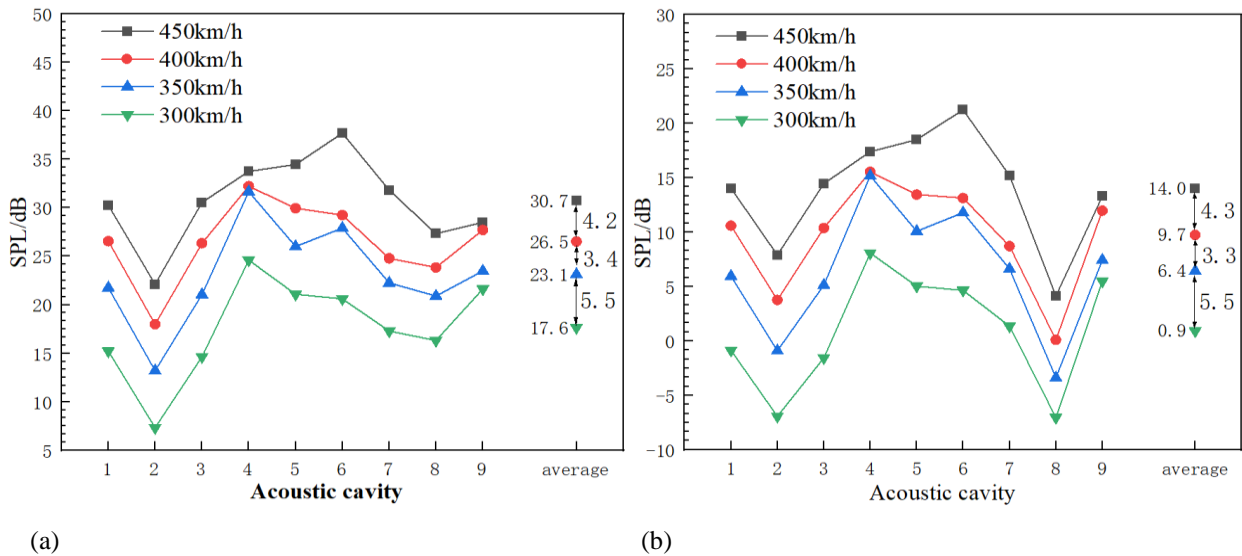
**Fig. 7 Overall SPL in each acoustic cavity (a) standing posture (b) sitting posture**

for the standing and sitting postures. Moreover, the average OSPL of the acoustic cavities on the horizontal plane increased with increasing speed for the standing and sitting postures. For example, the amplifications in the

horizontal plane for the standing posture are 5.5 dB (300–350 km/h), 3.4 dB (350–400 km/h), and 4.2 dB (400–450 km/h). A comparative analysis of Figs. 6(c) and (d) reveals that at the same train speed, the OSPL of the acoustic cavities at the standing posture level is greater than that at the sitting posture level.

5. ACTIVE JET REDUCTION METHOD FOR INTERIOR NOISE

The analyses presented above indicate that the turbulent pulsating pressure on the bottom of the pantograph cavity contributes to interior noise. The resulting vibration and noise are transmitted to the interior of the carriage via the roof, significantly affecting the comfort level underneath the pantograph. The interior noise must be reduced. Here, the TBL on the bottom of the pantograph cavity was disrupted, and the proposed active jet method was utilized in the pantograph cavity to mitigate the pulsating pressure. Moreover, during high-speed train operation, large and small vortices form in the pantograph cavity. As the speed increases, the vortex inside the cavity also increases. The active jet speed should be greater than the train speed to be able to control the vortex. Here, the jet velocities were 97.2 m/s (approximately 350 km/h), 111.1 m/s (approximately 400 km/h), 125 m/s (450 km/h), and 140 m/s (approximately 500 km/h). The active jet model utilized in this study is shown in Fig. 8. Sixteen jet holes were arranged in two rows (upper and lower rows) at the front end of the cavity. The diameter of each jet hole was 80 mm. The numerical simulation method employed in this study is described in Section 2.
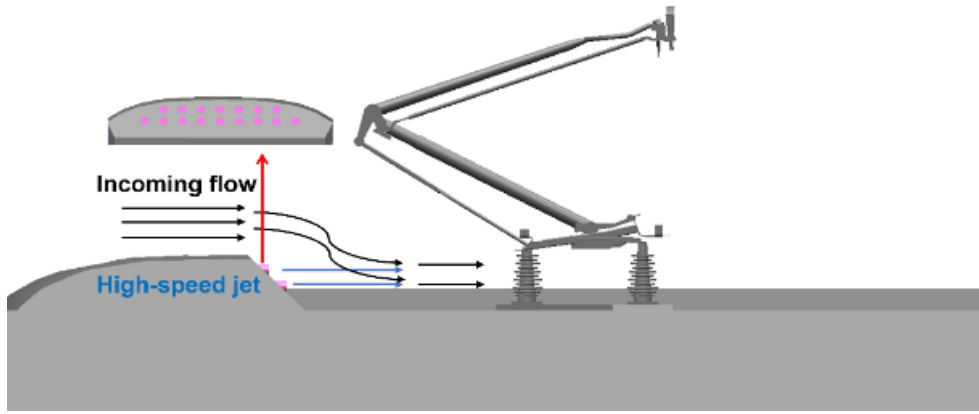
Fig. 8 Schematic of the jet model

(a) 300 km/h

(b) 350 km/h

(c) 400 km/h

(d) 450 km/h
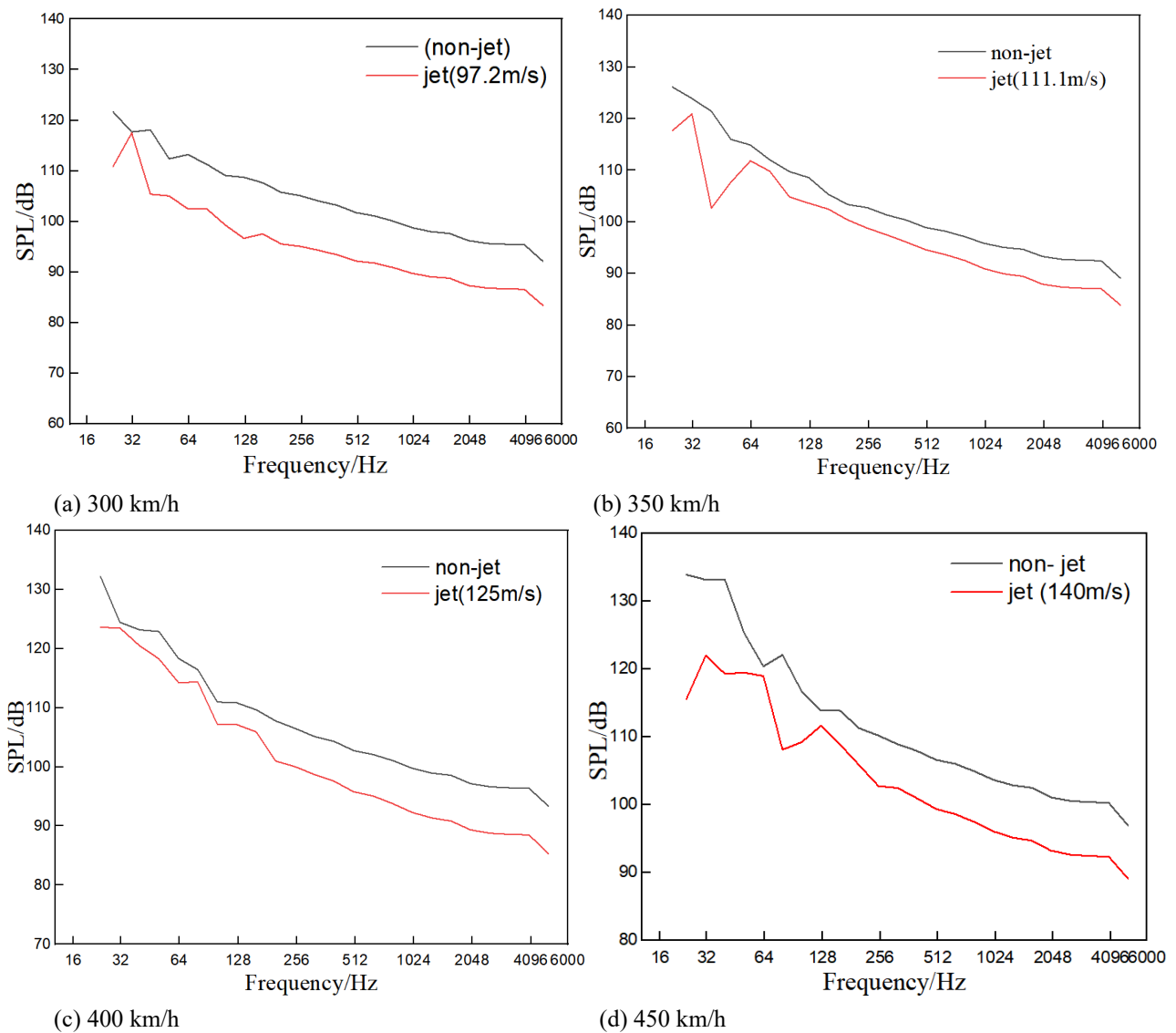
Fig. 9 Different train speeds and pulsating pressure spectra on back face 5 of the pantograph insulator with non-jet and jet mechanisms

Comparisons of the pulsating pressures between the simulation results for cavities with and without the active jet method are shown in Figs. 9(a) to (d). The pulsating

pressure of the insulator with positive rear face no. 5 decreased after implementing the active jet in the frequency range of 25–5000 Hz. In the low-frequency

range of 25–100 Hz, an amplitude change in the pulsating pressure during jet fluctuation was apparent. Within the frequency range of 100–5000 Hz, when the train speed was 300 km/h and the jet velocity was 97.2 m/s (Fig. 9[a]), the reduction in the pulsating pressure of face 5 was approximately 10 dB. When the train speed was 350 km/h and the jet velocity was 111.1 m/s (Fig. 9[b]), the reduction in the pulsating pressure in face 5 was approximately 5 dB. When the train speed was 400 km/h and the jet velocity was 125 m/s (Fig. 9[c]), the reduction in the pulsating pressure in face 5 was approximately 7 dB. When the train speed was 450 km/h and the jet speed was 140 m/s (Fig. 9[d]), the reduction in the pulsating pressure of face 5 was approximately 7 dB.

The four working conditions mentioned above indicate that the active jet aggravates the fluctuations in the pulsating pressure at the bottom of the cavity in the low-frequency band. However, in the full-frequency range, the active jet can effectively reduce the pulsating

pressure on the bottom and reduce the influence of the vortex inside the cavity.

The reduction effect of the active jet method on interior noise was evaluated. The pulsating pressure spectrum on the bottom of the pantograph cavity after implementing the active jet was incorporated into the SEA model. Figures 10 and 11 show the SPL spectrum of acoustic cavity no. 5, which is located in the horizontal plane for the standing and sitting postures. The decreasing trend in the SPL spectrum after active jet implementation was consistent with the analytical results under external conditions. Furthermore, even after the implementation of the active jet, the SPL spectrum of the acoustic cavity was greater for the standing posture than that for the sitting posture.

A comparative analysis of Figs. 10 and 11 indicates that when the vehicle speed is 300 km/h and the jet.

(a) 300 km/h

(b) 350 km/h

(c) 400 km/h

(d) 450 km/h
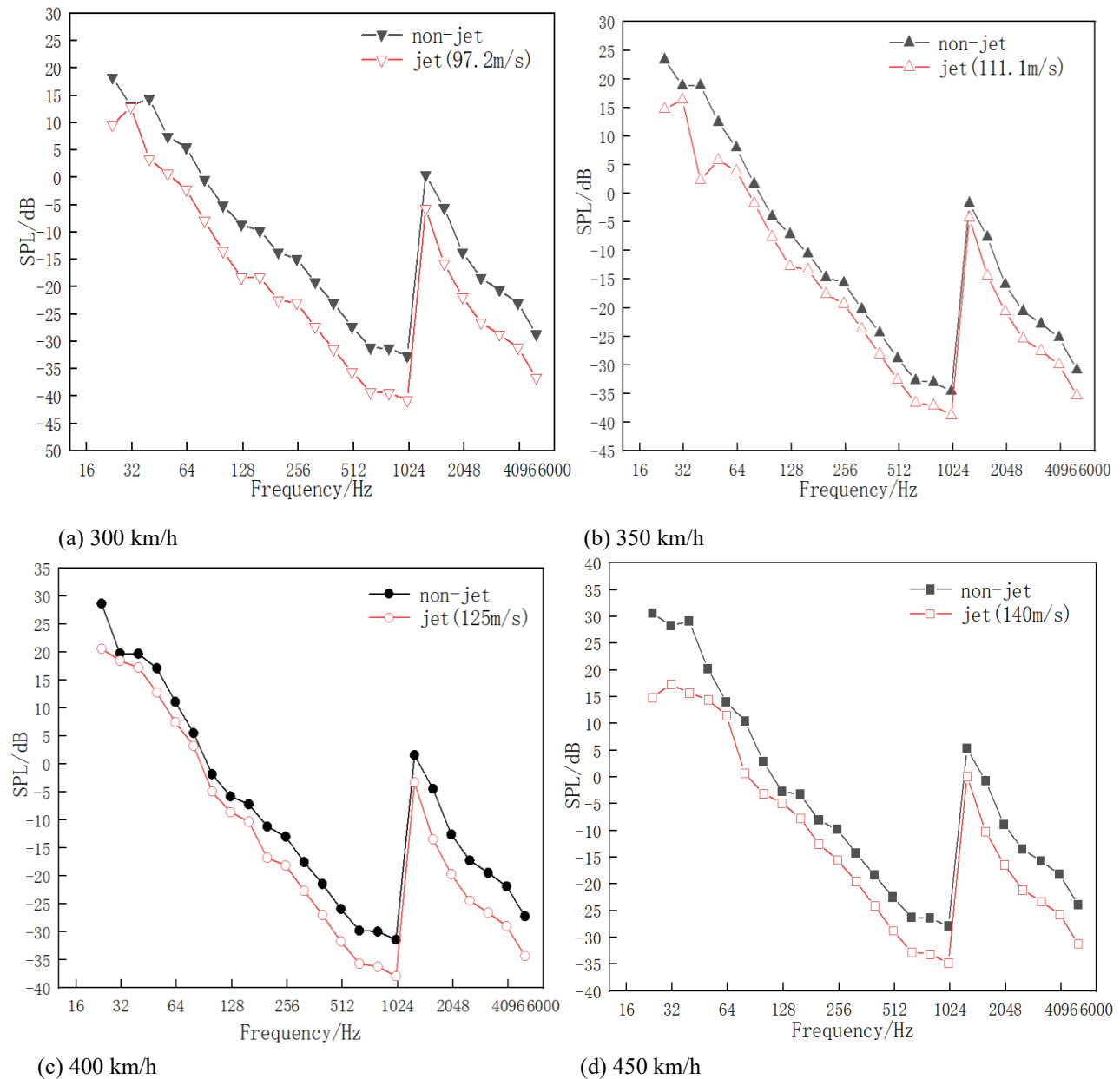
Fig. 10 Different train speeds and spectra of SPL in acoustic cavity 5 in the horizontal plane in the standing posture with non-jet and jet mechanisms

(a) 300 km/h

(b) 350 km/h

(c) 400 km/h

(d) 450 km/h
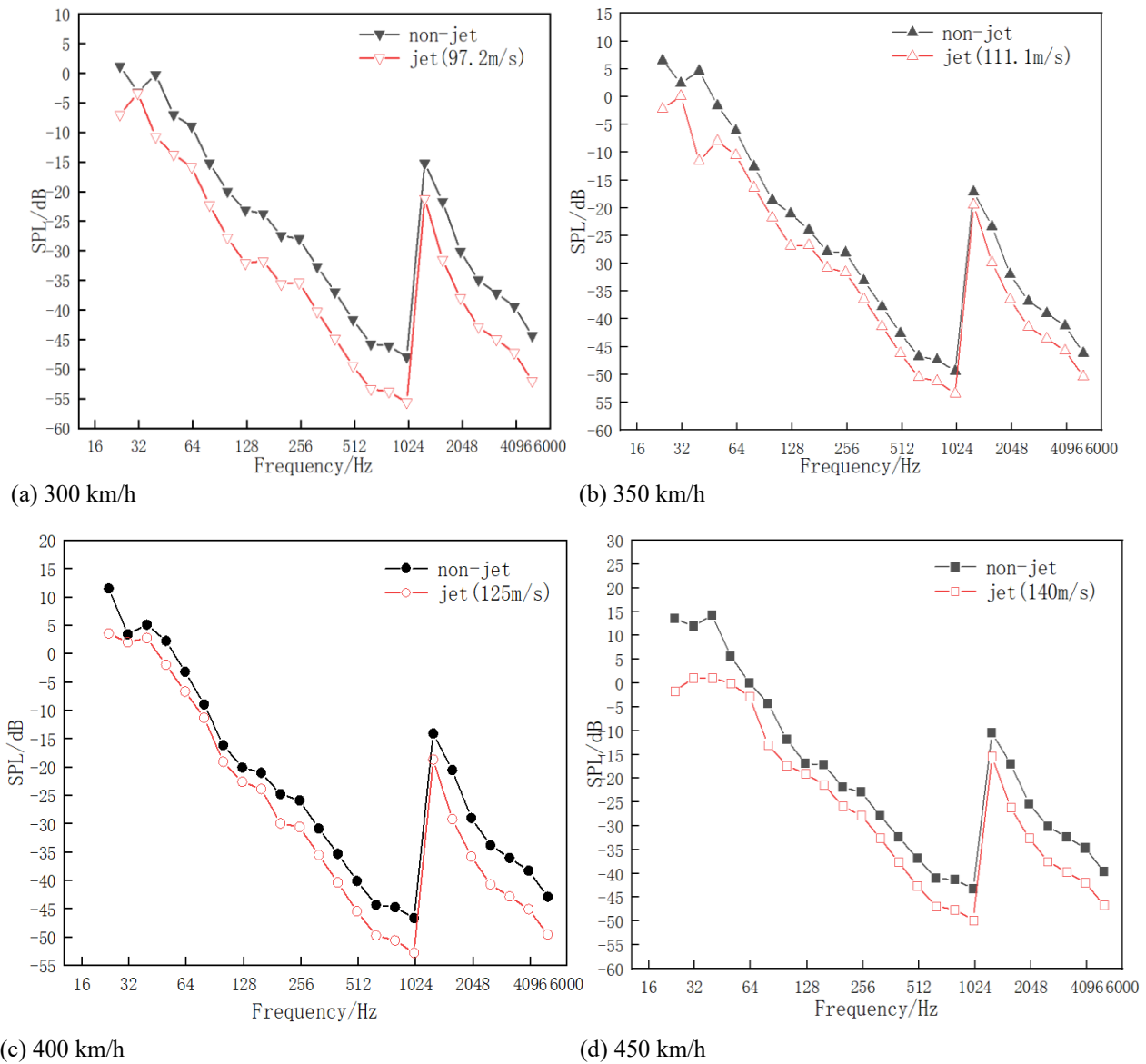
Fig. 11 Different train speeds and spectra of SPL in acoustic cavity 5 in the horizontal plane in the sitting posture with non-jet and jet mechanisms

velocity is 97.2 m/s, the sound pressure reduction in cavity no. 5 is 10 dB; this value is the same as that for the standing and sitting postures. When the speed was 350 km/h and the jet speed was 111.1 m/s (Figs. 10[b] and 11[b]), the reduction in cavity no. 5 was approximately 5 dB. When the vehicle speed was 400 km/h and the firing speed was 125 m/s (Figs. 10[c] and 11[c]), the reduction in cavity no. 5 was approximately 8 dB. When the vehicle speed was 450 km/h and the firing speed was 140 m/s (Figs. 10[d] and 11[d]), the reduction in cavity no. 5 was approximately 7

Figures 12 and 13 present a comparison of the OSPLs of the acoustic cavities on the horizontal planes for the standing and sitting postures, both before and after implementing the jet at various train speeds. When the train speed was 300 km/h and the jet velocity was 97.2 m/s (Figs. 12[a] and 13[a]), the average OSPL of each acoustic cavity in the horizontal plane for the standing and sitting postures decreased by 1.8 and 2.2 dB, respectively. When the train speed was 350 km/h and the jet velocity was 111.1 m/s (Figs. 12[b] and 13[b]), the average OSPL of each acoustic cavity in the horizontal plane for the

standing and sitting postures decreased by 4.5 and 4.8 dB, respectively. When the train speed was 400 km/h and the jet velocity was 125 m/s (Figs. 12[c] and 13[c]), the average OSPL of each acoustic cavity in the horizontal plane for the standing and sitting postures decreased by 4.2 and 4.1 dB, respectively. When the train speed was 450 km/h and the jet velocity was 140 m/s (Figs. 12[d] and 13[d]), the average OSPL of each acoustic cavity in the horizontal plane for the standing and sitting postures decreased by 7.5 and 7.6 dB, respectively.

Subsequently, the trends of interior noise at different speeds (Figs. 12 and 13) were compared and analyzed. The reduction in interior noise became more apparent when the train speed increased. This finding can be attributed to the increasing ratio of aerodynamic noise to train speed. Moreover, the active jet method achieved better noise reduction at higher speeds when the aerodynamic noise increased with increasing speed. On the basis of the analytical results, introducing an active jet in the pantograph cavity can effectively reduce the aerodynamic excitation source of the pantograph cavity and mitigate the interior noise in the pantograph region.

(a) 300 km/h

(b) 350 km/h

(c) 400 km/h

(d) 450 km/h
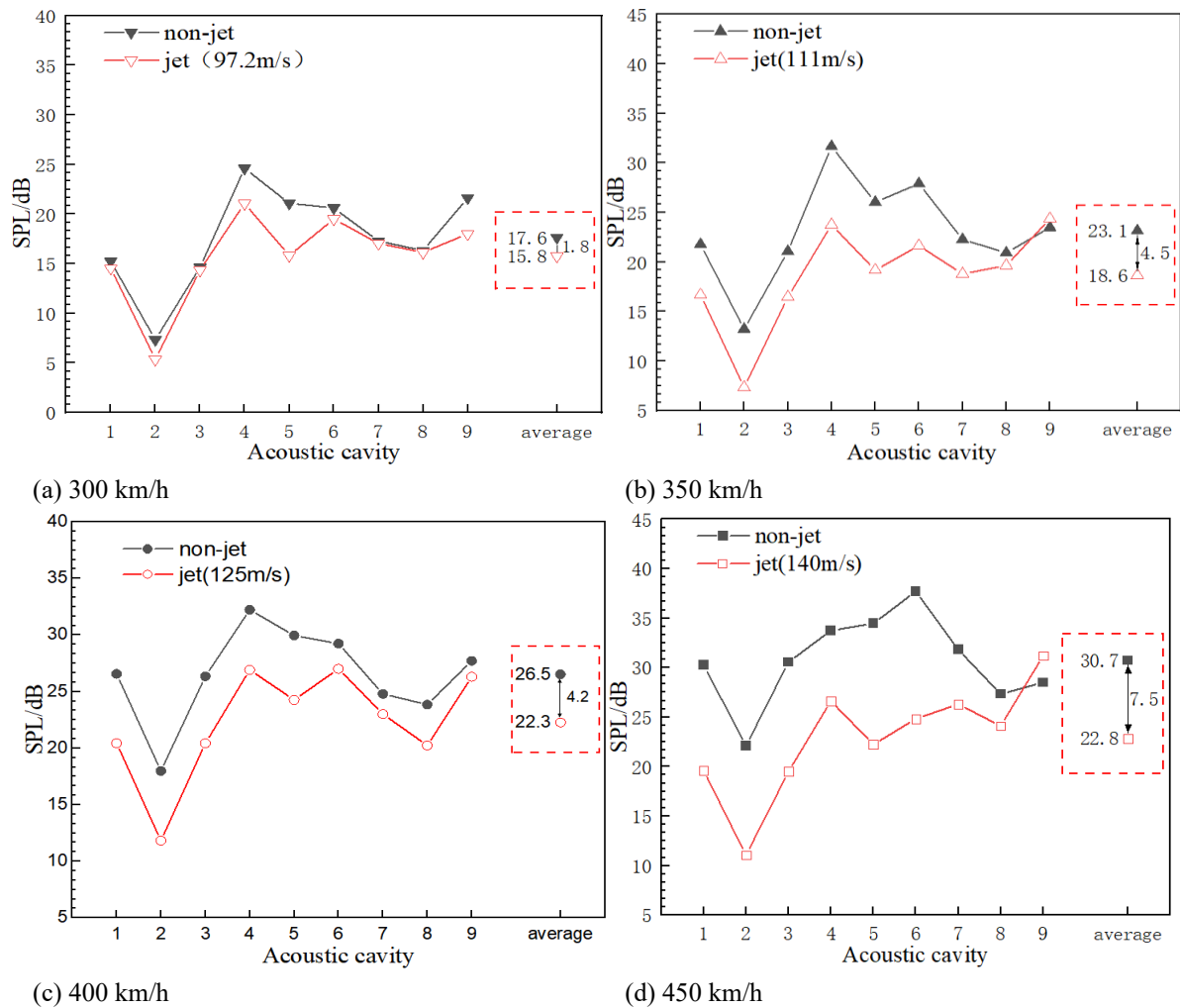
Fig. 12 Different train speeds and OSPL of each acoustic cavity in the horizontal plane of the standing posture with non-jet and jet mechanisms

At a speed of 350 km/h and a jet velocity of 97.2 m/s, the average OSPL of each cavity in the horizontal plane for both the standing and sitting positions can be reduced by 4.5 and 4.8 dB, respectively. Previously, Guo et al. (2017) proposed adding a conical oval structure vibration absorber between the pantograph insulator and the body to reduce the interior noise by 4 dB. Similarly, according to Zhang et al. (2014), when a layer of splint with a 0.01 m thickness and 0.5 loss factor is added to the original design in the carriage, the OSPL at the driver head location can be decreased by 1.23 dB (A). The results of the present study indicate that an active jet has a much better effect on noise control than other control methods.

6. CONCLSIONS

The focus of this research is interior noise. In this study, the active jet in the pantograph cavity was utilized to reduce the excitation source of aerodynamic noise (pulsating pressure). Consequently, interior noise control was achieved. The main conclusions of this research can be summarized as follows:

1. In the frequency range of 16–5000 Hz, the trend of the SPL in the train decreases with increasing frequency. However, in the area where the train and the external environment connect to each other, the sound insulation decreases, whereas the sound pressure in the train increases. The OSPL of the acoustic cavities in the horizontal plane positioned directly beneath the pantograph increases with increasing speed. In this work, the average OSPL for the standing posture increased by 5.6 dB (300–350 km/h), 3.7 dB (350–400 km/h), and 4.2 dB (400–450 km/h).

2. At different jet velocities and train speeds, the OSPLs of the acoustic cavities in the horizontal plane decrease for both the standing and sitting postures. In this work, at a speed of 300 km/h and a jet velocity of 97.2 m/s, the average OSPL of each cavity in the horizontal plane for both the standing and sitting positions is reduced by 1.8 and 2.2 dB, respectively. At a speed of 350 km/h with a jet velocity of 111.1 m/s, the average OSPL is reduced by 4.5 and 4.8 dB. At a speed of 400 km/h with a jet velocity of 125 m/s, the average OSPL decreases by 4.2 dB and 4.1 dB for the standing and sitting postures, respectively. Finally, at a speed of 450 km/h with a jet velocity of 140 m/s, the average OSPL decreases by 7.5 and 7.6 dB for the standing and sitting postures, respectively.

The results demonstrate the capability of the active jet to reduce interior noise in the pantograph area. The magnitude of the reduction increases with increasing train speed.

(a) 300 km/h

(b) 350 km/h

(c) 400 km/h

(d) 450 km/h
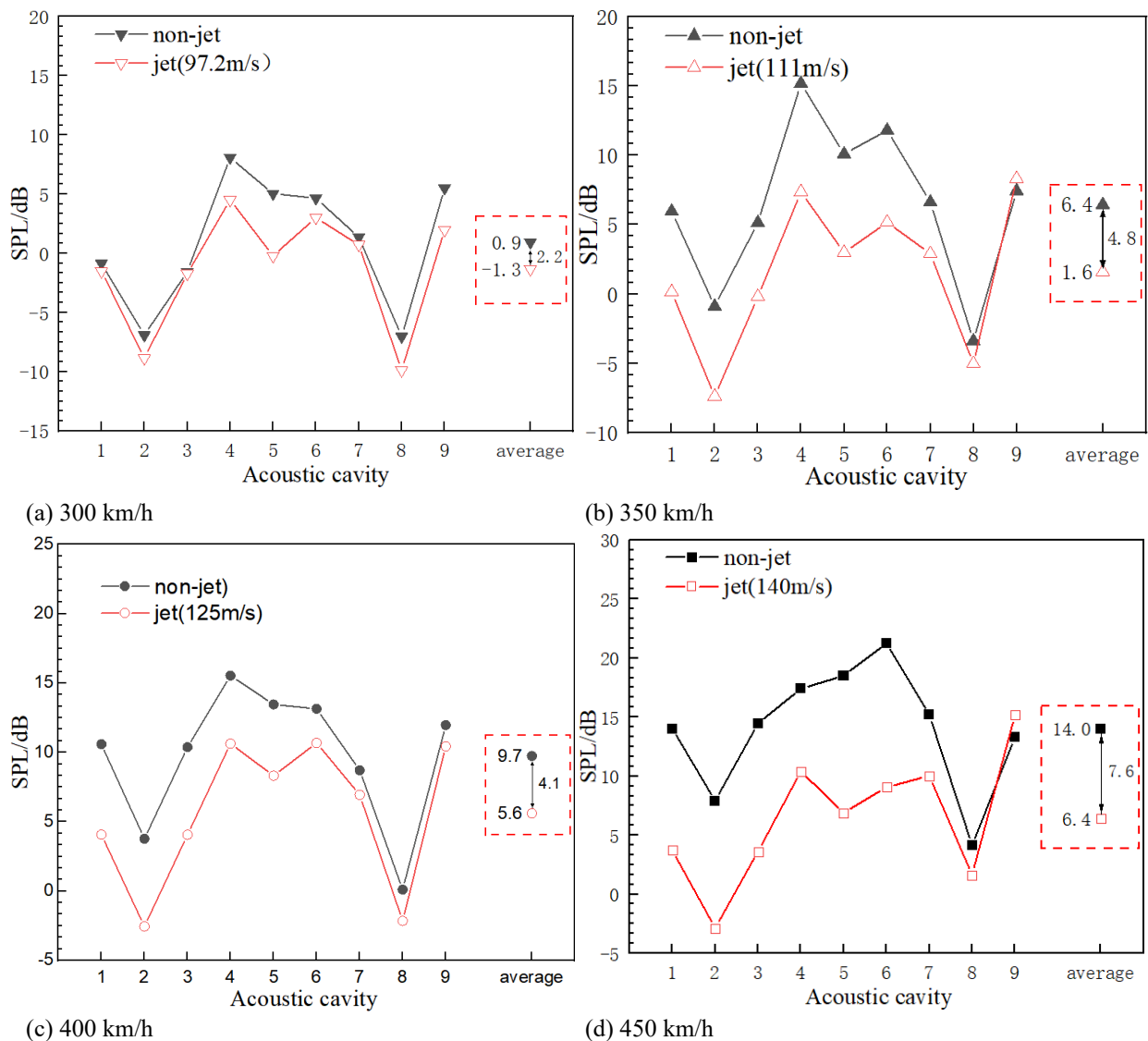
Fig. 13 Different train speeds and OSPL of each acoustic cavity in the horizontal plane of the sitting posture with non-jet and jet mechanisms

ACKNOWLEDGEMENTS

CONFLICT OF INTEREST

The authors declare that they have no known competing financial interests or personal relationships that could have appeared to influence the work reported in this paper.

AUTHORS CONTRIBUTION

All authors contributed to the study conception and design. D. Liu: data curation, investigation, software, visualization, formal analysis, and writing of original draft; **X. Miao:** visualization, methodology, and writing, review, and editing; **Z. Zhang:** resources and software; **J. Yang:** methodology, supervision, and review and editing; **T. Yuan:** methodology and supervision; **R. Song:** methodology and supervision.

REFERENCES

Burroughs, C. B., Fischer, R. W., & Kern, F. R. (1997). An introduction to statistical energy analysis. *The Journal of the Acoustical Society of America, 101*(4), 1779-1789. https://doi.org/10.1121/1.418074

Cao, Y., Bai, Y., & Wang, Q. (2018). Complexity simulation on application of asymmetric bionic cross-section rod in pantographs of high-speed trains. *Complexity*, 2018. https://doi.org/10.1155/2018/3087312.

Chen, Y. R., Xiao, Y. G., & Zhu, X. Y. (2016). Optimization of sound insulation performance of aluminum alloy profiles for EMU. *Rolling Stock, 54*(12), 11-15. (In Chinese). https://doi.org/10.3969/j.issn.1002-7602.2016.12.004

Chen, Z., Ge, J., Lin, J., Sun, Z., & Guo, J. (2012). Noise and vibration induced by a pantograph of high-speed trains. *The Journal of the Acoustical Society of America, 131*(4), 3264-3264. https://doi.org/10.1121/1.4708193

Guo, L., Xiao, D. M., & Jian, Y. (2023). Study on noise reduction of high-speed train pantograph by using jet device based on numerical simulation and wind tunnel test. *Journal of the China Railway Society, 45*(1), 20-27. https://doi.org/10.3969/j.issn.1001-8360.2023.01.003

Guo, J. Q., Ge, J. M., Sun, Z. J., Liu, S. Q., Zhao, Y. J., & Lin, J. S. (2017). Pantograph area noise and vibration transmission characteristics and interior noise reduction method of high-speed trains. In Noise and Vibration Mitigation for Rail Transportation Systems: Proceedings of the 11th International Workshop on Railway Noise, Uddevalla, Sweden, 9–13 September 2013 (pp. 563-570). Springer Berlin Heidelberg, https://doi.org/10.1007/978-3-662-44832-8_66

Henry, A., & Thebaud, J. C. (2016, August). *Create SEA predictive models to support building's acoustic design.* INTER-NOISE and NOISE-CON Congress and Conference Proceedings. https://www.ingentaconnect.com/contentone/ince/incecp/2016/00000253/00000006/art00077

Kim. T. M., & Kim, J. T. (2011). Comparison study of sound transmission loss in high speed train. *International Journal of Railway, 4*(1), 19-27. https://doi.org/10.7782/IJR.2011.4.1.019

Kolmogorov, A N. (1991). The local structure of turbulence in incompressible viscous fluid for very large Reynolds numbers. *Proceedings of the Royal Society of London. Series A: Mathematical and Physical Sciences, 434*(1890), 9-13. https://doi.org/10.1098/rspa.1991.0075.

Lee, S., Lee, S., & Cheong, C. (2022). Development of high-fidelity numerical methodology for prediction of vehicle interior noise due to external flow disturbances using LES and vibroacoustic techniques. *Applied Sciences, 12*(13), 6345. https://doi.org/10.3390/app12136345

Li, H., Liu, X., Thompson, D., & Squicciarini, G. (2022). The distribution of pantograph aerodynamic noise on train external surfaces and the influence of flow. *Applied Acoustics, 188*, 108542. https://doi.org/10.1016/j.apacoust.2021.108542

Li, Y., Xiao, X., Zhang, Y., Tang, Z., & Pan, A. (2023). Acoustic optimization design of porous materials on sandwich panel under flow-induced vibration. *International Journal of Aeroacoustics, 22*(1-2), 60-84. https://doi.org/10.1177/1475472X221150180

Lu, C., Ren, Z., & Ma, C. (2023). Study on the technologies development trend of high speed EMUs. *High-speed Railway, 1*(1), 1-5. https://doi.org/10.1016/j.hspr.2022.11.002

Schetz, J. A. (2001). Aerodynamics of high-speed trains. *Annual Review of Fluid Mechanics, 33*(1), 371-414. https://doi.org/10.1146/annurev.fluid.33.1.371

Thompson, D. J., Iglesias, E. L., Liu, X., Zhu, J., & Hu, Z. (2015). Recent developments in the prediction and control of aerodynamic noise from high-speed trains. *International Journal of Rail Transportation, 3*(3), 119-150. https://doi.org/10.1080/23248378.2015.1052996

Wang, X., Wang, T., Su, L., Wang, Y., Yang, D., Yang, C., & Liu, N. (2020). Adaptive active vehicle interior noise control algorithm based on nonlinear signal reconstruction. *Circuits, Systems, and Signal Processing, 39*, 5226-5246. https://doi.org/10.1007/s00034-020-01410-0

Yang, X. Y., Xiao, Y. G., & Sh, Y. (2013). Statistical energy analysis of wind noise in high-speed train cab. *Applied Mechanics and Materials, 249*, 307-313. https://doi.org/ConferenceArticle/5af2f5e2c095d70f18aaa750.

Yao, Y., Sun, Z., Li, G., Prapamonthon, P., Cheng, G., & Yang, G. (2022). Numerical investigation on aerodynamic drag and noise of pantographs with modified structures. *Journal of Applied Fluid Mechanics, 15*(2), 617-631. https://doi.org/10.47176/jafm.15.02.32849

Zhang, J., Xiao, X., Sheng, X., Zhang, C., Wang, R., Jin, X. (2016). SEA and contribution analysis for interior noise of a high speed train. *Applied Acoustics, 112*, 158-170. https://doi.org/10.1016/j.apacoust.2016.05.019.

Zhang, J., Yao, D., Peng, W., Wang, R., Li, J., & Guo, S. (2022). Optimal design of lightweight acoustic metamaterials for low-frequency noise and vibration control of high-speed train composite floor. *Applied Acoustics, 199*, 109041. https://doi.org/10.1016/j.apacoust.2022.109041

Zhang, J., Xiao, X., Sheng, X., & Li, Z. (2019). Sound source localisation for a high-speed train and its transfer path to interior noise. *Chinese Journal of Mechanical Engineering, 32*(1), 1-16. https://doi.org/10.1186/s10033-019-0375-1

Zhang, X. F., Xiao, Y. G., Sun, L., & Shi, Y. (2014). Aerodynamic noise reduction analysis in high-speed train cab. *Advanced Materials Research, 1049*, 1022-1025. https://doi.org/10.4028/www.scientific.net/AMR.1049-1050.1022

Zhu, J, Zhang, Q., Xu, F., Liu, L., & Sheng X. (2021). Review on aerodynamic noise of high-speed trains. *Journal of Traffic and Transportation Engineering in Chinese, 21*(3), 18. https://doi.org/10.19818/j.cnki.1671-1637.2021.03.003